JOURNAL OF THERMOPHYSICS AND HEAT TRANSFER
Vol. 12, No. 3, July–September 1998

Delta Clipper-Experimental In-Ground Effect on Base-Heating Environment

Ten-See Wang*
NASA Marshall Space Flight Center, Huntsville, Alabama 35812

A quasitransient in-ground effect method is developed to study the effect of vertical landing on a launch vehicle base-heating environment. This computational methodology is based on a three-dimensional, pressure-based, viscous flow, chemically reacting, computational fluid dynamics formulation. Important in-ground base-flow physics such as the fountain-jet formation, plume growth, air entrainment, and plume afterburning are captured with the present methodology. Convective and radiative base-heat fluxes are computed for comparison with those of a flight test. The influence of the laminar Prandtl number on the convective heat flux is included in this study. A radiative direction-dependency test is conducted using both the discrete ordinate and finite volume methods. Treatment of the plume afterburning is found to be very important for accurate prediction of the base-heat fluxes. Convective and radiative base-heat fluxes predicted by the model using a finite rate chemistry option compared reasonably well with flight-test data.

Nomenclature

C_p = heat capacity
C_1, C_2, C_3, C_μ = turbulence modeling constants, 1.15, 1.9, 0.25, and 0.09.
H = total enthalpy
h = static enthalpy
I = radiative intensity
J = Jacobian of coordinate transformation
K = molecular thermal conductivity
k = turbulent kinetic energy
M = molecular weight
N = total number of chemical species
P = pressure
Pr = Prandtl number
Q = heat flux, kW/m^2
q = 1, u, v, w, H, k, ε, or ρ_i
R = recovery factor or universal gas constant
S_q = source term for equation q
T = temperature, deg K
T^+ = nondimensional temperature
t = time, s
U = volume-weighted contravariant velocity
u, v, w = mean velocities in three directions
u_τ = wall friction velocity
u^+ = nondimensional velocity, (u/u_τ)
y^+ = nondimensional distance, $(y_p u_\tau \rho/\mu)$
ε = turbulent kinetic energy dissipation rate or wall emissivity
θ = heat transfer coefficient
κ = absorption coefficient
μ = effective viscosity, $(\mu_l + \mu_t)$
ξ = computational coordinates
Π = turbulent kinetic energy production
ρ = density
σ = scattering coefficient
σ_q = turbulence modeling constants
Φ = scattering phase function
ς = energy dissipation function
χ = molar fraction
$\boldsymbol{\Omega}$ = direction vector
ω = chemical species production rate

Subscripts

ad = adiabatic wall
b = blackbody
c = convective
l = laminar flow
p = off-wall (wall function) point
r = radiative
t = turbulent flow
w = wall surface

Introduction

THE Delta Clipper-Experimental (DC-X) vertical takeoff and landing (VTOL) rocket, built by McDonnell Douglas Aerospace (MDA) (Fig. 1), was developed to demonstrate a totally reusable launch vehicle. The descent portion of the trajectory requires unique flight maneuvers such as a retrothrust maneuver for deceleration and a powered vertical landing. These flight maneuvers of the four-engine DC-X induce a severe base-heating environment just prior to landing (the deployment of a deflector avoided base-heating concerns during liftoff). The definition of environments for this complex portion of flight is further complicated by the lack of applicable data. Early designers combined several one- and two-dimensional codes to solve a composite base flowfield and calculated a preflight plume-induced environment. The resultant preflight predictions for liftoff, ascent, rotation, retrothrust, and descent compared well to the measured flight data over most of the trajectory. However, during the critical landing phase, the predicted base-heat fluxes resulting from radiation and convection were both low relative to the data.

This paper seeks to improve the underprediction of the base-heat fluxes during landing caused by the engineering solution method by employing a computational fluid dynamics (CFD)-based unified thermoflowfield model. The finite difference Navier–Stokes (FDNS) code, which is the core of the model, has demonstrated abilities in computing the DC-X base-drag induced by the engine exhaust during flight,[1] base-pressure

---

Presented as Paper 97-2550 at the AIAA 32nd Thermophysics Conference, Atlanta, GA, June 23–25, 1997; received Oct. 6, 1997; revision received Jan. 6, 1998; accepted for publication Jan. 6, 1998.

*Team Leader, Fluid Dynamics Analysis Branch. Member AIAA.

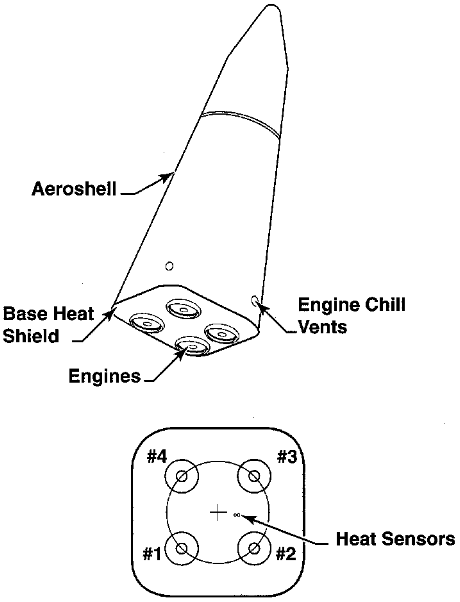

Fig. 1 Overall view of DC-X vehicle and base heat flux sensor location.

characteristic curve for a four-engine clustered nozzle configuration,[2,3] and heat transfer inside rocket thrust chambers[4] and coolant channels.[5] Experience gained from these calculations was used to develop a computational methodology based on a three-dimensional CFD formulation so that parametric computations could be performed to study the DC-X in-ground effect on base-heating environment.

The DC-X flight tests were designed partially to validate the CFD in terms of base heating. The computed heat fluxes are compared against those measured during a flight test for validation. A schematic of the DC-X vehicle and the location of the near base-center sensors at which the heat fluxes are compared is shown in Fig. 1.

In-Ground Base-Flow Physics

In this study the DC-X is assumed to be landing on a solid surface. Figure 2 shows the computed particle traces for the DC-X flowfield just prior to landing. It can be seen that the plume-to-ground impingement during DC-X landing generates two kinds of ground-jets: an outgoing ground-jet that rushes toward the ambient surroundings, and a center-converging ground-jet that converges under the DC-X and emerges as the fountain-jet. The direct impingement of the fountain-jet with the vehicle base is the source for the high-convective base-heating loads during landing. The pumping action of the nozzle exhaust plume entrains air that enables plume afterburning, adding to the convective base heating. Finally, because of the high concentration of steam in the hydrogen/oxygen plume and fountain-jet, an equally severe radiant heating component is also experienced by the base. After the fountain-jet-to-base impingement, a base wall-jet forms and rushes radially outward. The outward-rushing wall-jet and the outer ground-jet roll up to form large vortices that constitute the growth in exhaust-plume volume. It can be seen from Fig. 2 that all qualitative DC-X in-ground base-flow physics are represented with the computation. The effect of the engine-chill vent-jet is also included in the overall modeling for completeness, although it is shown in this study that it poses no threat to the base during landing on a solid surface because of small flow rate. Furthermore, a separate calculation showed that during landing on a grate-covered pit, the outgoing ground-jet is forced upward to potentially singe the side of the vehicle.

Quasitransient In-Ground Effect Method

During powered vertical descent, launch vehicles often encounter complex unsteady environments resulting from the interaction of the propulsive plumes, the ground, the base and airframe, and the prevailing winds. The interaction of the exhaust plume is felt by the vehicle when it is within two body-diameters of the ground.[6] Initially a slowdown is experienced, followed by a rapid suckdown starting about 70% of a body-diameter above the ground.[6] The vertical landing is therefore a transient process. However, it is impractical to simulate the actual transient process. A more computationally efficient quasitransient in-ground effect computational method is devised in this study and is based on two assumptions:

1) Because the base-center heat fluxes are expected to be the highest and are the least likely to be influenced by the prevailing winds as a result of the direct impingement of the fountain-jet and the formation of a diverging base wall-jet, the surrounding environment is assumed to be quiescent.

2) A specific landing point at which heating data are taken can be defined by three parameters, the landing altitude, descent speed, and engine condition. Based on these assumptions, a specific landing point corresponding to the peak base-heating environment during a flight test is chosen for this study. To perform the calculation, a time-marching solution is initiated by allowing the thrust chamber flow to exhaust into a quiescent environment, at time zero. In actual calculation, the vehicle is fixated in the computational domain, while the ground and air travel upwardly at the vehicle descending speed. As the calculation evolves, the propulsive plume develops, entrains air, afterburns, and impinges on to the ground. The fountain-jet forms and the subsequent in-ground physics develop. The computed base temperature and heat flux are monitored against elapsed time and the solution is time-marched to an asymptotic state. The heat fluxes obtained at the asymptotic state are compared against the measured peak heat fluxes and the simulation of an expensive, true transient-landing computation is thus avoided. In Fig. 1, the sensors are located close to but not at the base center, and near-base-center heat fluxes are referred to later in this paper.

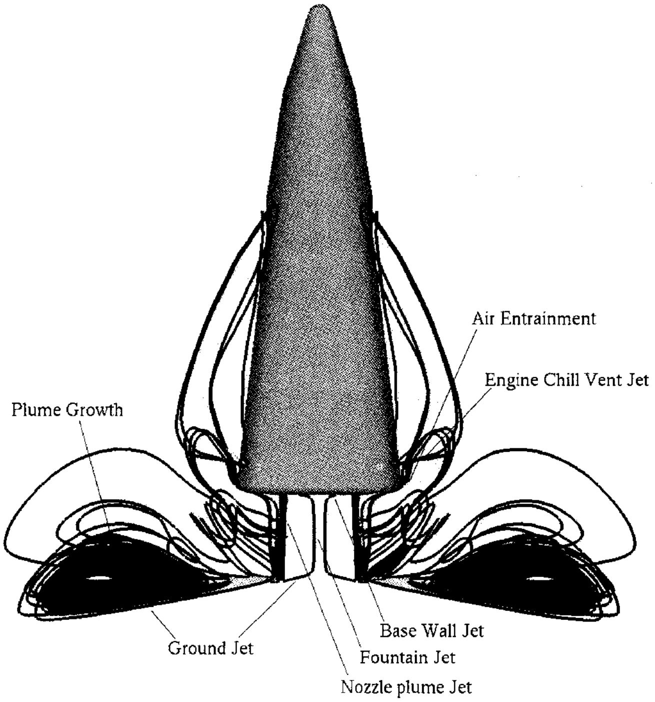

Fig. 2 Computed base flow particle traces during landing.

Solution Methodology

Computational Grid Generation

Extensive grid sensitivity study for base flows was performed in Refs. 2 and 3 for a four-engine clustered nozzle at

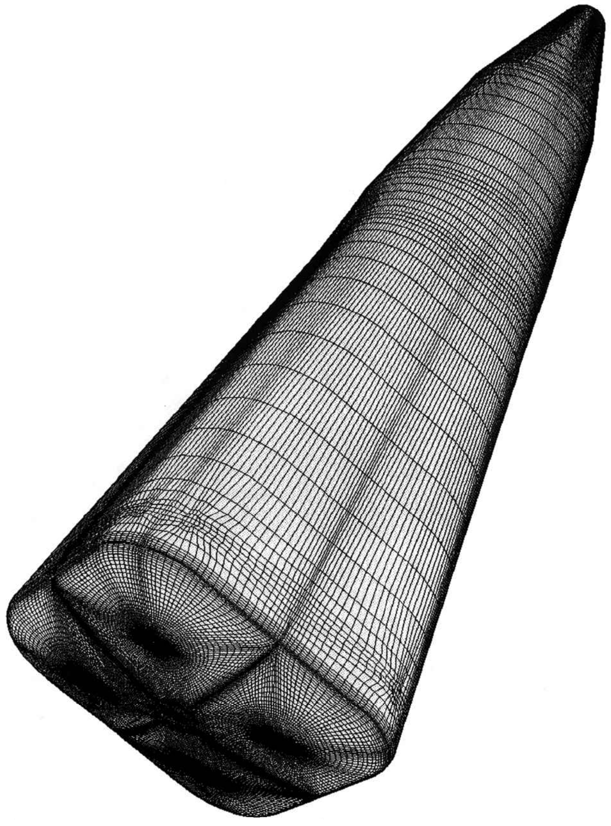

Fig. 3 **Layout of the DC-X surface computational grid.**

high altitudes, and was performed in Ref. 1 for DC-X cold-flow and flight tests at subsonic freestream speeds. In general, it was found that the sheer increase of the number of overall grid points, even when combined with solution-adaptive gridding, does not necessarily give a satisfactory result. In particular, it was found in Ref. 3 that local grid refinement such as the Prandtl–Meyer solution treatment for the near-nozzle-lip grid lines produces excellent results with a minimum number of grid points. It was also found in Ref. 1, for full-vehicle base-flow calculations and for subsonic freestream speeds, that higher grid density is required in the base and plume mixing layer regions but not in the forebody region. The demand increases with altitudes. The grid density requirement in the plume mixing layer is also higher for the afterburning plume than for the cold plume. In this work, the grid density and distribution were carefully designed using experience gained from those studies.[1–3] For example, grid lines near the nozzle lip were oriented according to the Prandtl–Meyer expansion. In fact, the grid used was originated from that used in Ref. 1 for the flight-test (with afterburning plume) case at the highest altitude (2800 m), except the axial distance from the base to the end of the computational domain (ground surface in this study) was shortened from 24 to 2 m. Because the grid density requirement for an altitude of 2 m is much less than that of 2800 m, the 12 times greater axial grid density makes this grid more than adequate. The grid was primarily generated with the GENIE++ grid generator,[7] except the base surface was created by projecting a two-dimensional grid layout onto the actual surface mapping, using the software package GRIDGEN.[8] A full view of the DC-X computational surface grid is shown in Fig. 3. In actual calculations, only one-eighth of the domain (408,288 points) is used because of flow symmetry assumptions. The same grid is used for both CFD and radiation calculations.

Convective Heat Flux

The FDNS CFD code is used to provide the basic general curvilinear coordinate, chemically reacting, transient viscous flowfield solution by solving the Reynolds-averaged transport equations. A generalized form of these equations is given by

$$\frac{\partial \rho q}{J \partial t} = \frac{\partial[-\rho U q + (\mu/\sigma_q) G (\partial q/\partial \xi)]}{\partial \xi} + \frac{S_q}{J} \tag{1}$$

A pressure-based predictor-plus-multicorrector solution method is formulated.[9] The basic notion is to correct the pressure and velocity fields by solving a pressure correction so that the velocity-pressure coupling is enforced, based on the continuity constraint. A second-order central-difference scheme is employed to discretize the diffusion fluxes and source terms of the governing equations. Extensive numerical-scheme sensitivity study was conducted for the convective terms in Ref. 1 for DC-X aerodynamic performance at subsonic flight regime and the second-order central-difference scheme was found to be superior to the other five schemes tested. Following that experience, the central-difference scheme is used in this study for DC-X landing in a quiescent environment.

An extended k-ε turbulence model[10] is used to describe the turbulence. The turbulence eddy viscosity is given by $\mu_t = \rho C_\mu k^2/\varepsilon$. Turbulence modeling constants σ_q and source terms S_q of the transport equations are given in Table 1. These turbulence modeling constants have been used extensively for combustion-driven and base flows,[1–5] whereas σ_k and σ_ε are taken from the turbulence closure.[10]

A modified wall function approach is employed to provide near-wall resolution that is less sensitive to the near-wall grid spacing. Consequently, the model has combined the advantages of both the integrated-to-the-wall approach and the conventional law-of-the-wall approach by incorporating a complete velocity profile[11] given by

$$\begin{aligned} u^+ &= \ell n[(y^+ + 11)^{4.02}/(y^{+2} - 7.37y^+ + 83.3)^{0.79}] \\ &\quad + 5.63 \tan^{-1}(0.12y^+ - 0.441) - 3.81 \end{aligned} \tag{2}$$

and a universal temperature profile[12] given by

$$T^+ = u^+ + 12.8(Pr_l^{0.68} - 1) \tag{3}$$

The convective heat transfer from a hot boundary layer to a cooler wall follows the modified Newtonian law

$$Q_{\mathrm{cw}} = \theta(h_w - h_{\mathrm{ad}}) = \theta[h_w - h_p - R(u_p^2/2)] \tag{4}$$

The heat transfer coefficient θ and recovery factor R from several investigators are listed in Table 2. Launder and Spal-

Table 1 σ_q and S_q of the transport equations

q	σ_q	S_q
l	1.00	0
u	1.00	$-P_x + \nabla[\mu(u_j)_x] - (2/3)(\mu\nabla u_j)_x$
v	1.00	$-P_y + \nabla[\mu(u_j)_y] - (2/3)(\mu\nabla u_j)_y$
w	1.00	$-P_z + \nabla[\mu(u_j)_z] - (2/3)(\mu\nabla u_j)_z$
H	0.95	$DP/DT + ς$
k	1.00	$\rho(\Pi - \varepsilon)$
ε	1.00	$\rho(\varepsilon/k)\{[C_1 + C_3(\Pi/\varepsilon)]\Pi - C_2\varepsilon\}$
ρ_i	1.00	ω_i, $i = 1, \ldots, N$

Table 2 Comparison of heat transfer coefficients and recovery factors

θ	R	Reference
$\rho u_\tau/[Pr_t(u^+ + B)]$	——	13
$\rho u_\tau/(Pr_t u^+)$	Pr_t	14, 15
$\rho u_\tau/T^+$	$Pr_l^{1/2}$	16
$\rho u_\tau/T^+$	$Pr_l^{1/2}$ if $y^+ \leq 11.63$ $Pr_l^{1/3}$ if $y^+ > 11.63$	This study

ding[13] developed the first expression for incompressible turbulent flows, where B is a function of laminar and turbulent Prandtl numbers. Viegas et al.[14] developed an improved heat transfer equation for compressible turbulent flows using the Reynolds analogy approach. The resulting function is applicable to attached and separated flows, to both high- and low-Reynolds flows, and to flows with adiabatic and nonadiabatic surfaces. This improved heat transfer equation was tested with a number of experiments, each with significant regions of flow separation. Chen et al.[15] subsequently reformulated it into a compact, yet mathematically equivalent form, where $Pr_t = 0.9$ was used as recovery factor for several supersonic film coolant flow tests. Chen et al.[16] later replaced the recovery factor with $Pr_l^{1/2}$, reasoning that the effect of the laminar boundary layer is more pronounced in the overall film heat transfer coefficient. Following van Driest,[17] the expression for the recovery factor is generalized depending on the flow regimes in this study, where $y^+ = 11.63$ is the thickness of the viscous sublayer.

Variable Laminar Prandtl Number

When a simple mixing rule, i.e., the mixture property is the sum of the individual species property multiplied by its molar fraction, is used for transport properties at the specified landing condition, Pr_l is 0.72 for air and Pr_l is 0.97 for the nozzle exhaust stream. Because of mixing of the plume with entrained air, the near-base Pr_l can therefore be bracketed between 0.72 and 1.0. However, because the near-wall universal temperature profile and recovery factor are both functions of Pr_l, it is instructive to determine the effect of a multicomponent Pr_l on the computed base heat fluxes. A variable laminar Prandtl-number formulation with a more accurate mixing rule is therefore in order.

The Chapman–Enskog formula[18] and Lennard–Jones potential[18] are used to calculate the molecular viscosities of the participating species, with the exception of polar species H_2O for which the Stockmayer potential[19] is used. Collision integrals are expressed as a function of the reduced temperature[18] and the force constants are obtained from Ref. 20. The polyatomic gas species thermal conductivity is related to viscosity and heat capacity through the formulation of Hirschfelder et al.,[18] and is given by

$$K = \frac{R\mu}{M}\left[3.75 + 1.32\left(\frac{C_p}{R} - 2.5\right)\right] \tag{5}$$

The two terms on the right-hand side represent the translational thermal conductivity caused by molecular translation motion and the internal thermal conductivity caused by the contribution of internal degrees of freedom of polyatomic molecules, respectively. Special correction coefficients for rotational motion are taken from Refs. 21 and 22. Wilke's semiempirical mixture-rule formula is used for improved multicomponent viscosity and thermal conductivity calculations[18]:

$$\Theta = \sum_{i=1}^{N}\left(\chi_i\Theta_i \Big/ \sum_{j=1}^{N}\chi_j\Psi_{ij}\right) \tag{6}$$

in which

$$\Psi_{ij} = \frac{1}{\sqrt{8}}\left(1 + \frac{M_i}{M_j}\right)^{-1/2}\left[1 + \left(\frac{\mu_i}{\mu_j}\right)^{1/2}\left(\frac{M_j}{M_i}\right)^{1/4}\right]^2 \tag{7}$$

where Θ can be either the mixture molecular viscosity or mixture molecular thermal conductivity. Notice that when $i = j$, $\Psi_{ij} = 1$. The computed transport properties were checked against several known multispecies mixtures and the comparisons were satisfactory. When the more accurate Wilke's formula was used as the mixing rule, the multicomponent Pr_l at the nozzle exit was calculated to be 0.76, much smaller than the 0.97 derived from the simple mixing-rule calculation. This finding narrows the near-base laminar Prandtl-number range from 0.72 to about 0.76.

Radiative Heat Flux

The general radiation solution program (GRASP)[23] is used to analyze the radiative field by solving the general curvilinear-coordinate radiative transfer equation (RTE):

$$(\boldsymbol{\Omega}\cdot\nabla)I(r,\boldsymbol{\Omega}) = -(\kappa + \sigma)I(r,\boldsymbol{\Omega}) + \kappa I_b(r) + \frac{\sigma}{4\pi}\int_{\Omega'=4\pi} I(r,\boldsymbol{\Omega}')\Phi(\Omega' \to \boldsymbol{\Omega})\,\mathrm{d}\boldsymbol{\Omega}' \tag{8}$$

where $\Phi(\boldsymbol{\Omega}' \to \boldsymbol{\Omega})$ is the scattering phase function from the incoming $\boldsymbol{\Omega}'$ direction to the outgoing $\boldsymbol{\Omega}$ direction. The term on the left-hand side represents the gradient of the intensity in the direction of $\boldsymbol{\Omega}$. The three terms on the right-hand side represent the changes in intensity because of absorption and out-scattering, emission, and in-scattering, respectively. The wall boundary is assumed gray while emitting and reflecting diffusely. Hence, the radiative wall boundary condition is given by

$$I(r_w,\boldsymbol{\Omega}^+) = \varepsilon I_b(r_w) + \frac{(1-\varepsilon)}{\pi}\int_{n\boldsymbol{\Omega}^-<0} I(r_w,\boldsymbol{\Omega}^-)|n\cdot\boldsymbol{\Omega}^-|\,\mathrm{d}\boldsymbol{\Omega}^- \tag{9}$$

with

$$q_{\mathrm{rw}} = \int_{n\boldsymbol{\Omega}^-<0} I(r_w,\boldsymbol{\Omega}^-)|n\cdot\boldsymbol{\Omega}^-|\,\mathrm{d}\boldsymbol{\Omega}^- \tag{10}$$

where $\boldsymbol{\Omega}^+$ and $\boldsymbol{\Omega}^-$ denote the leaving and arriving radiative intensity directions, respectively. Notice the angles of the leaving and arriving rays range from 0 to π, whereas the maximum angle of the incoming and outgoing directions in Eq. (8) is 4π. Two methods are used initially to solve the RTE: the discrete ordinate method (DOM) and the finite volume method (FVM). DOM solves the RTE along discrete directions that approximate the angular intensity distribution. A quadrature set associated with directions and weights is obtained by applying symmetry and moment matching conditions. In FVM the spatial domain is divided into a finite number of control volumes, and direction is divided into discrete control angles. The RTE is integrated over each control volume and control angle. In actuality, the discretized equation for the DOM is equivalent to that of the FVM when the discrete direction, the scattering phase function, and the weight are replaced with the averaged-intensity direction, the averaged-scattering phase function, and the control angle.[23] Relative to the DOM, the FVM has advantages of freedom in control angle selection and guarantee of radiant energy conservation. Liu et al.[23] benchmarked these two methods on problems with transparent, absorbing, emitting, and scattering mediums. The results are similar for both methods in terms of accuracy and computational time, although the FVM held slight advantage over DOM in some cases. Details of the general curvilinear coordinate formulations for both methods can be found in Ref. 23. A 20-band spectral-line weighted-sum-of-gray-gases (SLWSGG) model[24] is used to calculate the total emissivity and absorptivity of the radiating medium. The SLWSGG model, unlike the original four-band weighted-sum-of-gray-gases (WSGG) model that is not suitable for a nonisothermal, nonhomogeneous environment, is based on an absorption-line blackbody distribution function, which is generated and fitted empirically from detailed spectral line data. This function accounts for the variation of Plank's function over the entire spectrum, requiring only a single integration over the absorption cross section. Hence, the SLWSGG model provides an efficient radiative transfer calculation in a high-temperature system with accuracy approaching that of more costly line-by-line techniques. Discussion of the comparison of SLWSGG model with other radiation absorption models can be found in Ref. 24.

Boundary and Initial Conditions

The outer boundary of the computational domain is comprised of two symmetry planes, one ground surface, and the remaining planes that are flow exits. No-slip walls are specified for the DC-X and the ground surfaces. Backflow is allowed for the flow exit planes, and ambient total properties are used. A fixed (ambient) static pressure is imposed on a point far away from the vehicle/ground interaction area, to obtain a unique solution for the specified landing altitude. The ground and entire initial flowfield are given the DC-X landing speed with a direction opposite to the descending vehicle. A fixed inlet boundary condition is applied to the nozzle exit plane where the flowfield variables are mapped from a separate axisymmetric CFD thrust chamber solution. That separate calculation was started from the subsonic chamber, to ensure the correct nozzle exhaust flow properties, including internal boundary-layer growth, nozzle shock strength and location, and turbulence level. The subsonic chamber inlet-flow properties were obtained from a thermoequilibrium analysis[25] using engine conditions. This procedure of performing a separate thrust chamber calculation is crucial to the final solution because the propulsive nozzle flow is the source of the base-flow physics.[1]

For base-convective heat transfer calculations, an apparent difficulty is that the heat flux depends also upon the unknown base surface temperature. Two methods are commonly used in engineering practice. The first is a conjugate heat transfer method[4] that iterates the surface temperature by balancing the hot-gas-side base-heat flux with that inside of the base aeroshell; however, this is impractical for a preliminary design stage. An alternative method is simply to prescribe the local surface temperature.[5] In this study ambient temperature is prescribed as the base surface temperature like that used by the engineering method, whereas adiabatic wall is specified for all other surfaces, including the ground surface.

Results and Discussion

The time-marching flow computations were performed on the NASA Marshall Space Flight Center CRAY T-90. The computational time for a typical frozen chemistry calculation was estimated as 4.8×10^{-5} CPU s/grid/step, whereas the computational time for a typical finite rate chemistry calculation is 1.6×10^{-4} CPU s/grid/step. The radiation computations were performed on the NASA Marshall Space Flight Center J-90 CRAY, where the computational time for a typical run is approximately 6.5×10^{-5} CPU s/grid/step/direction.

Figure 4 shows the computed temperature history at ground and base centers. The base-center temperature is monitored at the off-surface grid point (wall function point) because the surface temperature is fixed. The frozen chemistry flow case was performed first. It can be seen that the ground-center temperature rises sharply at around 0.02 s, corresponding to the time of convergence of the ground-jet and of emergence of the fountain-jet. At around 0.05 s, the mature fountain-jet impacts the base center, causing its temperature to rise sharply. The frozen chemistry solution reaches an approximate asymptotic state at around 0.13 s at both base and ground centers. Three finite rate chemistry cases then follow with different Prandtl-number specifications: 0.72, variable, and 1.0. A seven-species, nine-reaction detailed mechanism[26] was used to describe the finite rate, hydrogen–oxygen afterburning kinetics. Of the seven species H_2, O_2, H_2O, O, H, OH, and N_2, the only radiating medium is H_2O. After the initialization of the chemical reactions, it can be seen that the temperatures increase some 850 K immediately before leveling off at both locations. This dramatically illustrates the importance of including plume afterburning in the calculation. The temperature profiles of $Pr_l = 0.72$ and variable Pr_l appear to be overlapping each other, indicating the near-base-center Prandtl number is probably very close to 0.72. The eventual convergence to similar values of all three finite rate cases, in spite of the difference in Prandtl numbers, indicates overall energy conservation of the present computational method.

Figure 5 shows the computed base-convective heat-flux histories at the sensor location. The characteristic times of fountain-jet initiation, fountain-jet-to-base impingement, and afterburning initialization are identical to those described in Fig. 4. The frozen flow heat flux reaches an asymptotic value of 440 kW/m^2 at around 0.13 s and is much lower than those of the finite rate chemistry cases. Nearing their asymptotic-states, the variable Pr_l heat-flux profile is approximately bracketed by those of $Pr_l = 0.72$ and $Pr_l = 1.0$ and almost coincides with that of $Pr_l = 0.72$. Unlike the temperature histories shown in Fig. 4, the final heat flux of $Pr_l = 1.0$ case does not approach those of the two other cases. This is because the sensors are not located at the geometrical center of the base and the flow properties around the sensors, e.g., the heat transfer coefficients, vary with the Prandtl number.

The comparison of the final computed near-center base-convective heat fluxes against flight-test data is shown in Table 3. The data are reduced by subtracting the measured heat flux of radiometer from that of total calorimeter. The frozen-flow calculation gives the worst comparison at −40% error. All of the finite rate chemistry solutions give a reasonable comparison, regardless of the difference in Prandtl numbers. The importance of the afterburning effect on the convective base-heating prediction is obvious.

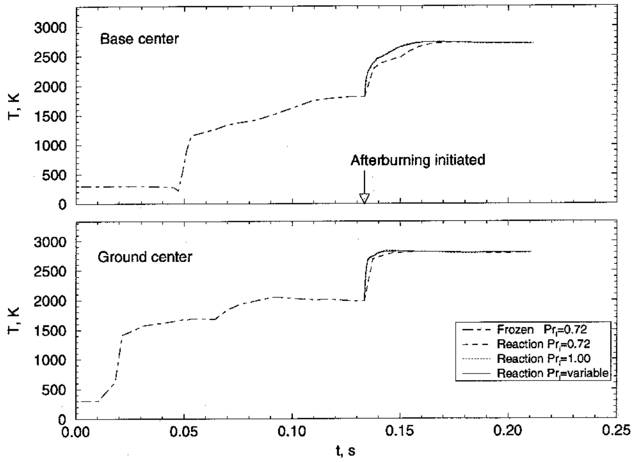

Fig. 4 Computed ground- and base-center temperatures.

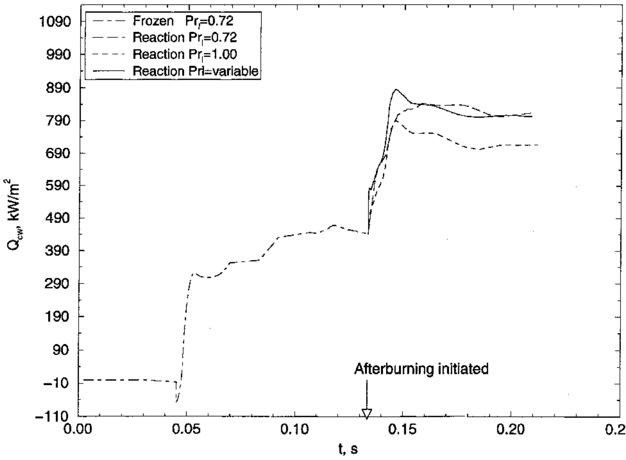

Fig. 5 Computed base-convective heat fluxes.

Table 3 Heat-flux comparison

	Pr_t	Q_{cw}(Err%)	Q_{rw}(Err%)
Test data	——	738	397
Finite rate	0.72	829(12)	374(−0.05)
Finite rate	Variable	806(9)	397(0.00)
Finite rate	1.00	704(−5)	397(0.00)
Frozen	0.72	442(−40)	79(−80)

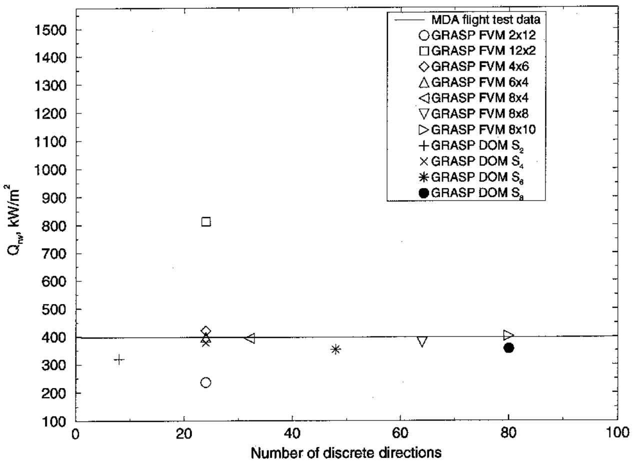

Fig. 6 Parametric study of the computed radiative base heat fluxes.

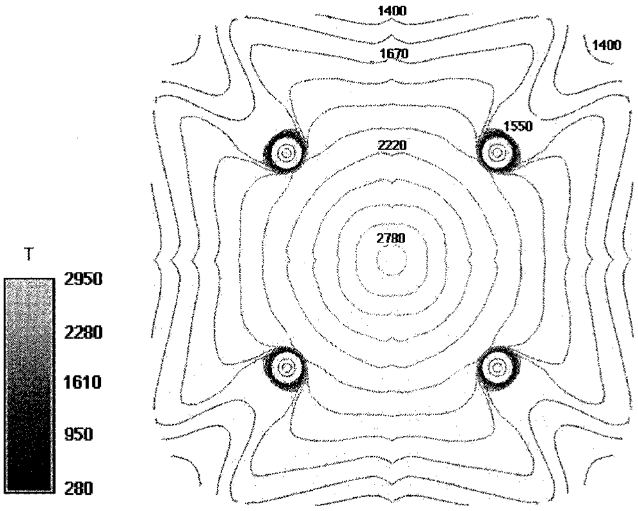

Fig. 7 Base-temperature contours using variable Prandtl number.

In radiative heat-flux calculations, a radiative direction dependency study is first performed for the reacting $Pr_t = 0.72$ case to determine the most efficient method and to avoid the ray effect. From Fig. 6, the agreement between the prediction and test data appear to improve with an increased number of beam directions, albeit the improvement becomes marginal when the total number of rays exceeded 32. Overall, the FVM solutions hold a slight edge over those of DOM, agreeing with the benchmark findings of Ref. 23. The optimal solution appears to occur with the FVM 6 × 4 method, although the DOM S_4 solution is also good. The FVM 6 × 4 method is therefore chosen for the subsequent calculations. The FVM 6 × 4 method has six control angles in the polar direction and four in the azimuthal direction. It should be noted that the DOM S_4 quadrature scheme is equivalent to the FVM 4 × 6 and 6 × 4 in terms of the number of beam directions (24) used. Also the solution of the FVM 12 × 2 is much worse than that of the FVM 6 × 4, emphasizing the importance of appropriate beam distribution rather than the sheer number of beams. The final comparison for the near-center base-radiative heat fluxes are also shown in Table 3. Again, the frozen flow case gives the worst comparison at −80% underprediction, whereas all of the finite rate chemistry cases yield excellent comparison to the measured data.

The contours of the base temperature, radiative heat flux, convective heat flux, and Prandtl number for the reacting flow, variable Pr_t case are shown in Figs. 7–10. It can be seen that, as expected, the peak temperature and radiative heat flux occur at the base center. The peak base-convective heat flux occurs off base center because of the complicated flow physics of fountain-jet-to-base impingement, stagnation point, and incipient base wall-jet formations. Reference 27 reported that the highest heating rate for a 1/25 scale, three-engine, J-2 nozzle model occurs at the base center for lower altitudes (30–40 km) and at an off-base-center location for higher altitudes (44–80 km). The agreement of the trend in base heat-flux distribution for DC-X landing and for J-2 nozzle model operating at high altitudes indicates that the effect of a maximum-heating fountain-jet-to-base impingement is similar to that of a strong reverse-jet-to-base impingement, although the formation mechanism of a reverse-jet[2,3] is different from that of a fountain-jet. The reverse-jet also forms at lower altitudes for a clustered-engine configuration, albeit at a weaker strength. The peak Pr_t

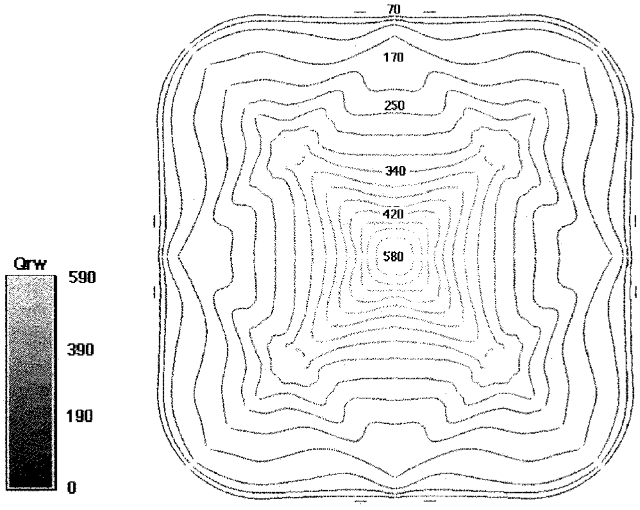

Fig. 8 Base-radiative heat flux contours using variable Prandtl number.

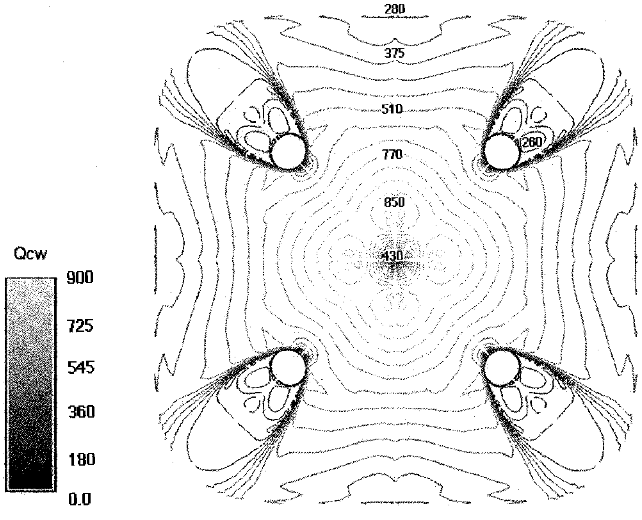

Fig. 9 Base-convective heat flux contours using variable Prandtl number.

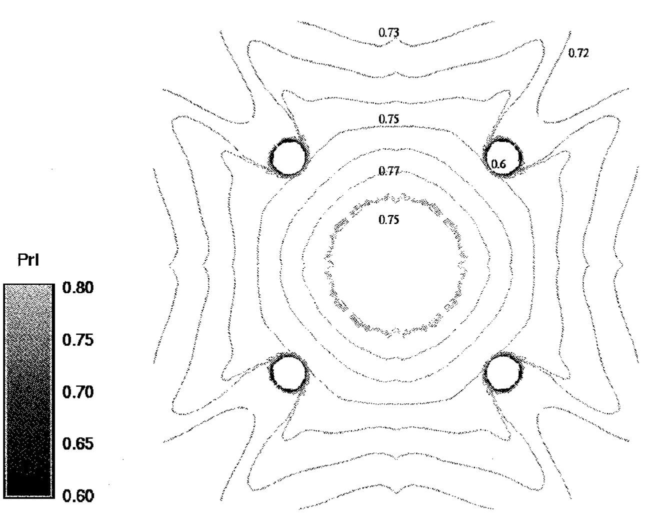

Fig. 10 Base Prandtl-number contours.

also occurs at an off-base-center location. This is because the multicomponent Pr_t is a complicated function of species concentration, molecular weight, and laminar transport properties. As a result the temperature effect is less pronounced on the Pr_t contours. From base center to the approximate sensor location, Pr_t only varies from 0.75 to 0.77, indicating that the near-base-center wall-jet essentially shields itself from the influence of the entraining air. Inside the recirculating flow region formed by the wall-jet flowing past the exhaust plume, lower values of temperature, base-convective heat flux, and Prandtl number result. That secondary flow, however, has far less effect on the base radiative heat flux, because view factor plays a major role in radiative transport.

The parametric study of Prandtl numbers indicates that for the base-heating prediction purpose, the use of a constant Prandtl number is probably as good as using a more sophisticated variable Prandtl-number formulation. However, the added computational cost in performing a variable Prandtl-number calculation is negligible because only wall-function points are involved. The most significant parameter for an accurate base-heating prediction is the afterburning of the unburned plume fuel with the entrained air. Without inclusion of the plume afterburning effect, the base heat-flux underpredictions can be as much as 40% for the convection and 80% for the radiation, respectively.

Conclusions

A CFD-based computational design methodology is developed to predict the severe radiative and convective heating environments experienced by base region components during the landing maneuver of a vertical-landing vehicle using clustered engines. All of the important in-ground base-flow physics such as the ground-jet convergence, fountain-jet formation, base wall-jet development, air entrainment, and plume afterburning have been captured by the present methodology. The predicted heat fluxes using finite rate chemistry compared very well with those of measurement, indicating the importance of plume afterburning in base-heating predictions.

Acknowledgment

The author wishes to thank Scott Ward of McDonnell Douglas Aerospace for suggesting the project and for providing technical assistance.

References

[1] Wang, T.-S., and Cornelison, J., "Analysis of Flowfields over Four-Engine DC-X Rockets," *Journal of Spacecraft and Rockets*, Vol. 34, No. 5, 1997, pp. 620–627.

[2] Wang, T.-S., "Numerical Analysis of Base Flowfield for a Four-Engine Clustered Nozzle Configuration," *Journal of Propulsion and Power*, Vol. 11, No. 5, 1995, pp. 1076–1078.

[3] Wang, T.-S., "Grid-Resolved Analysis of Base Flowfield for Four-Engine Clustered Nozzle Configuration," *Journal of Spacecraft and Rockets*, Vol. 33, No. 1, 1996, pp. 22–29.

[4] Wang, T.-S., and Luong, V., "Hot-Gas-Side and Coolant-Side Heat Transfer in Liquid Rocket Engine Combustors," *Journal of Thermophysics and Heat Transfer*, Vol. 8, No. 3, 1994, pp. 524–530.

[5] Wang, T.-S., and Chyu, M. K., "Heat Convection in a 180-Deg Turning Duct with Different Turn Configurations," *Journal of Thermophysics and Heat Transfer*, Vol. 8, No. 3, 1994, pp. 596–601.

[6] Cooper, J. A., Fanciullo, T., Parsley, R., and Dalsem, W. V., "Future Single-Stage Rockets: Reusable and Reliable," *Aerospace America*, Feb. 1994, pp. 18–20.

[7] Soni, B. K., Thompson, J. F., Stokes, M. L., and Shih, M.-H., "GENIE++, EAGLE View and TIGER: General and Special Purpose Interactive Grid Systems," AIAA Paper 92-0071, Jan. 1992.

[8] Steinbrenner, J. P., and Chawner, J. R., "The GRIDGEN Version 8 Multiple Block Grid Generation Software," MDA Engineering Rept. 92-01, Arlington, TX, 1992.

[9] Wang, T.-S., and Chen, Y.-S., "Unified Navier-Stokes Flowfield and Performance Analysis of Liquid Rocket Engines," *Journal of Propulsion and Power*, Vol. 9, No. 5, 1993, pp. 678–685.

[10] Chen, Y.-S., and Kim, S. W., "Computation of Turbulent Flows Using an Extended k-ε Turbulence Closure Model," NASA CR-179204, Oct. 1987.

[11] Liakopolous, A., "Explicit Representations of the Complete Velocity Profile in a Turbulent Boundary Layer," *AIAA Journal*, Vol. 22, No. 6, 1984, pp. 844–846.

[12] White, F. M., *Viscous Fluid Flow*, McGraw–Hill, New York, 1974.

[13] Launder, B. E., and Spalding, D. B., "The Numerical Computation of Turbulent Flows," *Computational Methods in Applied Mechanics and Engineering*, Vol. 3, No. 2, 1974, pp. 269–289.

[14] Viegas, J. R., Rubesin, M. W., and Horstman, C. C., "On the Use of Wall Functions as Boundary Conditions for Two-Dimensional Separated Compressible Flows," AIAA Paper 85-0180, Jan. 1985.

[15] Chen, Y.-S., Cheng, G.-C., and Farmer, R. C., "Reacting and Non-Reacting Flow Simulation for Film Cooling in 2-D Supersonic Flows," AIAA Paper 92-3602, July 1992.

[16] Chen, Y.-S., Shang, H.-M., Liaw, P., Cheng, G.-C., Farmer, R. C., and Chen, C.-P., "Numerical Simulation of Film Cooling Effectiveness in a Combustor Chamber," *Proceedings of Pacific International Conference on Aerospace Science and Technology*, Vol. III, National Cheng Kung Univ., Taiwan, ROC, 1993, pp. 1258–1265.

[17] Van Driest, E. R., "The Problem of Aerodynamic Heating," *Aeronautical Engineering Review*, Vol. 15, No. 10, 1956, pp. 26–41.

[18] Hirschfelder, J. O., Curtis, C. F., and Bird, R. B., *Molecular Theory of Gases and Liquids*, Wiley, New York, 1954.

[19] Monchick, L., and Mason, E. A., "Transport Properties of Polar Gases," *Journal of Chemical Physics*, Vol. 35, No. 5, 1961, pp. 1676–1697.

[20] Svehla, R. A., "Estimated Viscosities and Thermal Conductivities of Gases at High Temperatures," NASA TR R-132, 1962.

[21] Heimerl, J. M., and Coffee, T. P., "The Detailed Modeling of Premixed, Laminar Steady-State Flames," *Combustion and Flame*, Vol. 39, No. 1, 1980, pp. 301–305.

[22] Warnatz, J., "The Structure of Laminar Alkane-, Alkene-, and Acetylene Flames," *18th International Symposium on Combustion*, The Combustion Inst., Pittsburgh, PA, 1981, pp. 369–383.

[23] Liu, J., Shang, H.-M., Chen, Y.-S., and Wang, T.-S., "Prediction of Radiative Transfer in General Body-Fitted Coordinates," *Numerical Heat Transfer*, Pt. B, Vol. 31, 1997, pp. 423–439.

[24] Liu, J., Shang, H.-M., Chen, Y.-S., and Wang, T.-S., "GRASP: A General Radiation Simulation Program," AIAA Paper 97-2559, June 1997.

[25] Svehla, R. A., and McBride, B. J., "FORTRAN IV Computer Program for Calculation of Thermodynamic and Transport Properties of Complex Chemical Systems," NASA TN D-7056, Jan. 1973.

[26] Wang, T.-S., McConnaughey, P., Chen, Y.-S., and Warsi, S., "Computational Pollutant Environment Assessment from Propulsion System Testing," *Journal of Spacecraft and Rockets*, Vol. 33, No. 3, 1996, pp. 386–392.

[27] Hand, A. E., McKay, G. B., and Fuller, C. E., "Short Duration Base Pressure and Heat Transfer Test of 1/25 Scale, 3 Engine, J-2 Nozzle Model," Engineering Rept. 1551, Hayes International Corp., Birmingham, AL, Nov. 1968.